Blind Deblurring Using Space Target Features

PEIYU LIU [1], **YAN ZHAO** [1], **(Member, IEEE), WENBO YANG** [1,2],
SHIGANG WANG [1], **AND SHU CHEN** [1,3]
[1]College of Communication Engineering, Jilin University, Changchun 130012, China
[2]Changchun Observatory of National Astronomical Observatories Academy of Science, Changchun 130117, China
[3]Special Police College of the PAP, Beijing 102211, China

Corresponding author: Yan Zhao (zhao_y@jlu.edu.cn)

ABSTRACT The star image suffers inevitably from degradation due to the high-speed motion of the space
target and the long exposure time of the camera, therefore the attitude information of the star is hard to
accurately obtain. This paper proposes a blind deblurring algorithm that combines shape features of space
targets. First, the astronomical image is preprocessed using saliency detection. Then, considering the shape
characteristics of space targets, the Minimum Bounding Rectangle (MBR) is introduced to describe the
space targets. Next, the parameters of the MBR are used to estimate the point spread function (PSF).
Finally, a regularization method is employed to recover the astronomical images. Experimental results
on both simulation and real star images demonstrate that the proposed method reduces the error of point
spread function estimation and decreases the error rate of identified space targets. At the same time, the
accuracy of the star centroid extraction improves 0.2786 on average and the error of the star centroid location
extraction reduces 0.059 comparing to the state-of-art method. The proposed method is of great significance
for positioning, recognition and attitude determination of space targets.

INDEX TERMS Blind deblurring, minimum bounding rectangle, point spread function, star image restoration.

I. INTRODUCTION

With the further study of human beings in the field of deep
space exploration, the quality requirements for star images
are getting higher and higher. Space targets are man-made
targets including spacecraft and space debris [1]. Since most
of the targets are passive, passive detection equipment is
widely used for observation. The detection of the Mid-
dle Earth Orbit (MEO) space targets is mainly achieved
by ground-based optoelectronic telescopes with star sen-
sors [2], [3]. A star tracker, also known as star sensor,
is a high-precision, autonomous attitude measurement device,
which can carry out attitude estimation without prior informa-
tion and does not drift with time. It is widely used in various
types of spacecraft [4].

Typically, the attitude of satellite is determined by the fol-
lowing steps: star image preprocessing, star centroid extrac-
tion, star identification [5], attitude estimation [1]. When
observing and identifying space targets, obtaining the basic
parameters and physical features are the key to observation.

The attitude accuracy of the star sensor mainly depends on
the accuracy of the star centroid. Therefore, the star image
processing of the star sensor before centroiding is very sig-
nificant to the attitude accuracy of the star sensor. Under
static conditions, star image processing steps usually include
background noise removal, binary operation and connected
component analysis [6]. However, compared with the static
situation, the star images captured under dynamic conditions
are no longer distributed in a Gaussian distribution [7], but
scattered in a long trail, which is seriously blurred. The space
target is moving at high speed, moreover, the exposure time
of the star sensor is long. Therefore, it has relative motion
with the camera. Slight movement may cause the star image
to be elongated and blurred. Coupled with the effects of
atmospheric turbulence [8], photon shot noise, readout noise,
and dark current noise, the signal to noise ratio (SNR) of the
star images will drop and the degradation of the star image is
more serious, which makes the star centroid [9]–[11] shift and
blur, even seriously affects the normal attitude of the space
target. Therefore, the restoration of the star image directly
determines the efficiency of the observation and the accuracy
of the detection.

The associate editor coordinating the review of this manuscript and
approving it for publication was Larbi Boubchir.

Our study aims to design a deblurring method to solve the above problems. Our paper is organized as follows. The introduction is given in Section 1 and the related work is given in Section 2. The proposed method is described in detail in Section 3. The experiment results are given in Section 4, and the conclusion is drawn in Section 5.

II. RELATED WORK

Image restoration is introduced into star image in the 1960s. Nathan [12] proposes inverse filtering for obtaining clear satellite images. Now, image restoration has been widely used in various astronomical fields [13], such as image reconstruction observed to IRAS (Infrared Astronomical Satellite) [14], revealing the internal structure of the mid-infrared image processing of active galactic nucleus NGC 1068 [15], and eliminating telescope tracking errors [16]. In order to estimate the fuzzy kernel, McGlamery deconvolutes the image in [17]. However, this method is sensitive to noise and the restoration results are not satisfactory. To solve this problem, a Wiener filter is proposed in [18]. Wu and Wang [19] and Zhang *et al.* [20] discuss the degradation models and corresponding PSFs, and they propose the constrained least square filter and Wiener filter for star image restoration, however this method may easily cause the ringing effect. Sun *et al.* [21] use the traditional Richardson-Lucy (RL) algorithm to effectively remove the ringing effect. However, the method is carried out in the case of known point spread function (PSF). Moreover, the accuracy of the restored star image is not satisfactory due to the equality of the deblurring star points. On the basis of the RL algorithm, an attitude-correlated frames (ACF) method to improve the accuracy of attitude acquisition is further studied in [22]. The ACF method associates the attitudes of adjacent frames. For existing algorithms, the PSF of the blurred star image can be obtained by the gyroscope and satellite attitude information [2], [19], [21], [23], [24] or estimated by isolated star point [25]. Wang *et al.* [26] propose a method to calculate blur kernel, aided by a MEMS gyroscope. To improve the performance of the star sensor under dynamic conditions, Liu *et al.* [27] propose a gyroscope-assisted star image prediction method and an improved Richardson-Lucy (RL) algorithm based on the ensemble back-propagation neural network (EBPNN). A method of star image under dynamic conditions which is effective in the motion-blurred star image processing is discussed in [28] and [29], and it is adaptive to different dynamic conditions. Zhao *et al.* [30] propose an improved median filtering and fast blind restoration method, which can effectively remove noise and restore the star image, but the energy of star points is not particularly concentrated. However, ideal navigation images are different from natural images, since most pixels of the navigation images are zero and only a small amount of pixels contains beacon or star spot information [25]. Ramos *et al.* [31] leverage deep learning techniques to significantly accelerate the blind deconvolution process and produce corrected images at a peak rate of ∼100 images per second. This method can produce excellent image corrections with noise suppression while maintaining
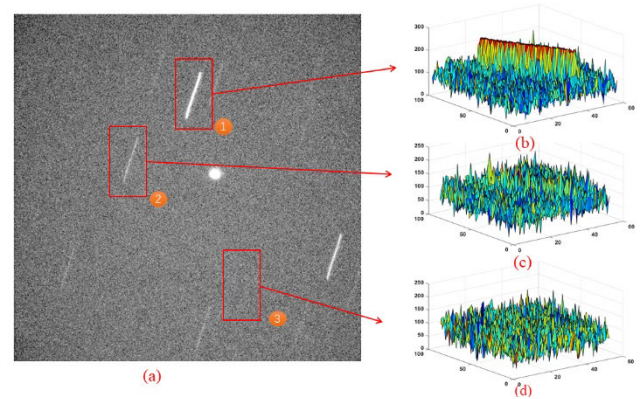

FIGURE 1. An example of a blurred star image and the 3D image intensity profiles of its local areas; (a)Original star image;(b) Histogram of region ①; (c) Histogram of region ② (d) Histogram of noise region ③.

the photometric properties of the images. However, a large training set with annotation is necessary in this method.

Krishnan and Fergus [32] propose a regularization method for image restoration, which is greatly affected by noise. The noise case can be addressed by introducing a regularization term into the objective function to avoid noise amplification [33]. Sparse representation is utilized to remove the Poisson-Gaussian mixed noise of the low-resolution star image [34]. However, the methods are complex for obtaining the PSF.

Therefore, the estimation of the PSF becomes one of the key issues in the restoration of blurred star images.

III. PROPOSED METHOD

Fig. 1 shows an example of a blurred star image and the 3D image intensity profiles of its local areas. Fig.1 (a) is the original star image. Fig.1 (b) and (c) are the 3D image intensity profiles of regions ① and ② in (a), which contain space targets with different sizes, and (d) is the 3D image intensity profiles of noise region ③. From the 3D profile images, it can be seen that the original star images have more noise and scattered star points, which makes it difficult to identify and fix the attitude. Figure 2 shows the block diagram of the proposed method. The original star image is preprocessed using saliency detection first. Then, the space target is identified using MBR and the point spread function is estimated based on motion length estimation and motion angle estimation. Finally, the star image is deblurred by a regularization method.

A. STAR IMAGE PREPROCESSING

The star image has obvious noise due to the influence of skylight, photon and electron of the camera. Therefore, the preprocessing of star images and saliency detection [35], [36] will be more helpful to subsequent star image restoration.

The histogram of the original star image is shown in Fig.3. It can be seen that the pixel points are mainly concentrated within the gray value from 0 to 80, and the distribution is uneven. There is little difference between the light and dark
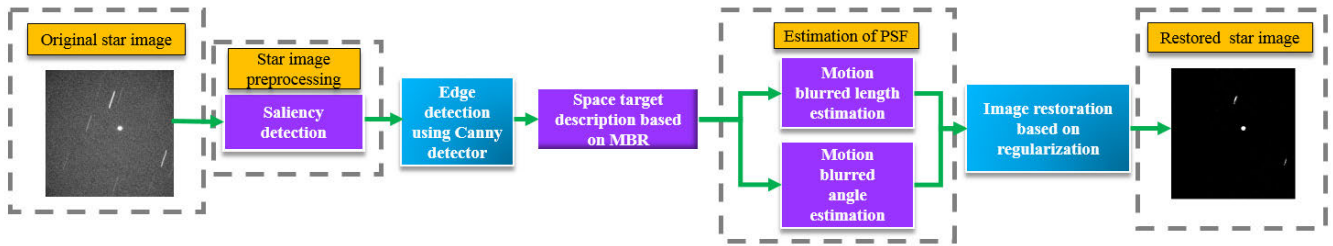
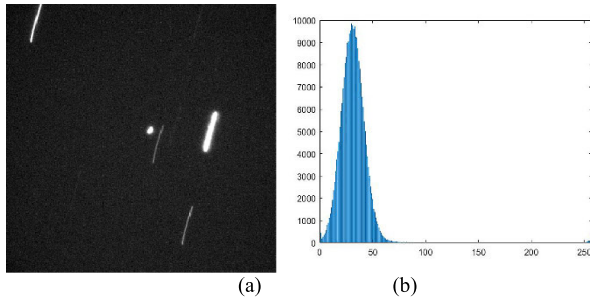**FIGURE 2.** Block diagram of the proposed method.

FIGURE 3. Histogram of a star image.

changes of the target, and it is difficult to carry out target recognition and deblurring. Therefore, saliency detection of star image is necessary. The mean of pixel values is used to calculate the significance due to the high brightness of space targets such as MEO relative to the background starry sky. The saliency image $H(x, y)$ is obtained by

$$H(x, y) = \begin{cases} \dfrac{S_1(x, y) - S_{min}}{S_{max} - S_1(x, y)} & (S_1(x, y) \neq S_{max}) \\ 255 & (S_1(x, y) = S_{max}) \end{cases} \quad (1)$$

where $S_1(x, y)$ is the square of the difference between the pixel of the image and the arithmetic mean, which is calculated by (2), S_{min} is the minimum value of $S_1(x, y)$, S_{max} is the maximum value of $S_1(x, y)$ which are given by (3) and (4) respectively.

$$S_1(x, y) = (I(x, y) - \mu)^2 \quad (2)$$

$$S_{min} = min(S_1(x, y)) \quad \begin{cases} x = 1, 2, \ldots, M - 1 \\ y = 1, 2, \ldots, N - 1 \end{cases} \quad (3)$$

$$S_{max} = max(S_1(x, y)) \quad \begin{cases} x = 1, 2, \ldots, M - 1 \\ y = 1, 2, \ldots, N - 1 \end{cases} \quad (4)$$

where μ is the arithmetic mean of the pixel of the star image, $M \times N$ is size of the image $I(x, y)$. After saliency detection, the contrast between the space target and background is increased. In addition, the background noise is removed, and only the space targets are retained.

B. SPACE TARGET DESCRIPTION BASED ON MINIMUM BOUNDING RECTANGLE

After the saliency detection, the contrast between the star spot and the background is improved, and there is almost no noise

interference. Our method is to study and restore a certain space target. The objects we concern are motion blurred MEO space targets. We restore the space targets for accurate positioning and tracking. After a long exposure time, the motion blurred length is large, and the space target is obvious, which is helpful to edge detection. Therefore, the Canny operator is used for edge detection for the preprocessed star image and the outline of each target can be obtained. Space target often has the shape of a bar due to the relative motion between space target and the camera, therefore the space target is described by MBR in our paper.

Given n boundary points (x_i, y_i) $i = 1, 2, \ldots, n$ of a space target, the centroid $(\bar{x}, \bar{y})$ of the boundary can be given by (5):

$$(\bar{x}, \bar{y}) = \left(\frac{1}{n} \sum_{i=1}^{n} x_i, \frac{1}{n} \sum_{i=1}^{n} y_i \right) \quad (5)$$

As shown in Fig.4, l_1 is a line passing through the centroid which is defined by (6), where θ is the angle between l_1 and the horizontal axis.

$$l_1: (y - \bar{y}) - tan\,\theta\,(x - \bar{x}) = 0 \quad (6)$$

The perpendicular distance from the edge point (x_i, y_i), $i = 1,2,3, \ldots, n$ to the line l_1 is

$$p_i = (x_i - \bar{x}) sin\,\theta - (y_i - \bar{y}) cos\,\theta \quad (7)$$

The sum of square of the perpendicular distance of each edge point (x_i, y_i) is defined by

$$P = \sum_{i=1}^{n} [(x_i - \bar{x}) sin\,\theta - (y_i - \bar{y}) cos\,\theta]^2 \quad (8)$$

In order to calculate the angle θ, we minimize P respect to θ. Therefore, $\frac{\partial P}{\partial \theta} = 0$ gives

$$tan\,2\theta = \frac{2 \sum_{i=1}^{n} (x_i - \bar{x})(y_i - \bar{y})}{\sum_{i=1}^{n} \left[(x_i - \bar{x})^2 - (y_i - \bar{y})^2 \right]} \quad (9)$$

The major axis of MBR l_1 can be obtained as shown in Fig.4, and the line perpendicular to the major axis is the minor axis l_2 which is defined by

$$l_2: (y - \bar{y}) + cot\,\theta\,(x - \bar{x}) = 0 \quad (10)$$

Consequently, the directions of the major and minor axes can be determined.
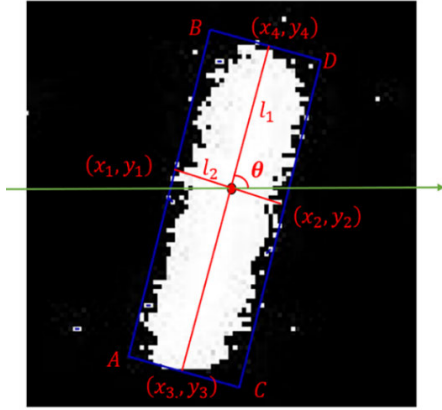
FIGURE 4. The illustration of an MBR.

As shown in Fig.4, the four intersection points between MBR, the major axis and minor axis are (x_1, y_1), (x_2, y_2), (x_3, y_3), (x_4, y_4) respectively. And the four vertices of the MBR are determined as follows

$$A : (a_x = \frac{x_1 \tan \theta + x_3 \cot \theta + y_3 - y_1}{\tan \theta + \cot \theta},$$
$$a_y = \frac{y_1 \cot \theta + y_3 \tan \theta + x_3 - x_1}{\tan \theta + \cot \theta}) \quad (11)$$

$$B : (b_x = \frac{x_1 \tan \theta + x_4 \cot \theta + y_4 - y_1}{\tan \theta + \cot \theta},$$
$$b_y = \frac{y_1 \cot \theta + y_4 \tan \theta + x_4 - x_1}{\tan \theta + \cot \theta}) \quad (12)$$

$$C : (c_x = \frac{x_2 \tan \theta + x_3 \cot \theta + y_3 - y_2}{\tan \theta + \cot \theta},$$
$$c_y = \frac{y_2 \cot \theta + y_3 \tan \theta + x_3 - x_2}{\tan \theta + \cot \theta}) \quad (13)$$

$$D : (d_x = \frac{x_2 \tan \theta + x_4 \cot \theta + y_4 - y_2}{\tan \theta + \cot \theta},$$
$$d_y = \frac{y_2 \cot \theta + y_4 \tan \theta + x_4 - x_2}{\tan \theta + \cot \theta}) \quad (14)$$

C. ESTIMATION OF POINT SPREAD FUNCTION

Image restoration can be regarded as the inverse process of image degradation. In frequency domain, the relationship between the blurred image $G(u, v)$ and the original image $F(u, v)$ is

$$G(u, v) = F(u, v) H(u, v) + N(u, v) \quad (15)$$

where $N(u, v)$ represents Fourier transform of noise, and $H(u, v)$ is the fuzzy kernel, which is Fourier transform of the point spread function. In a short exposure time T, the relative motion between the space target and the astronomical camera can be considered as a uniform linear motion. Given $x_0(t)$ and $y_0(t)$ be the motion components of the space target along horizontal and vertical directions respectively, the $H(u, v)$ is given by

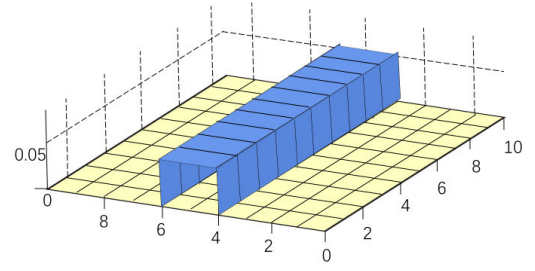$$H(u, v) = \int_0^T exp\{-j2\pi [(ux_0(t) + vy_0(t)]\}dt \quad (16)$$

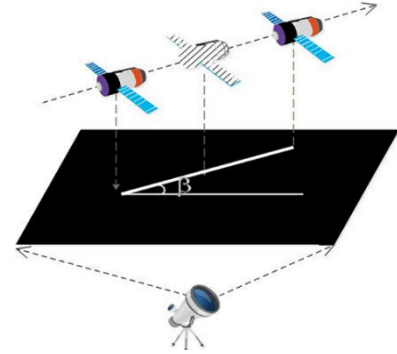**FIGURE 5.** A point spread function model.

FIGURE 6. Motion angle of blurred image.

Since the actual blurred star image is a digital image, the (16) should be transformed to its discrete form, which is

$$H(u, v) = T \frac{sin \left(\pi \left(\frac{uL sin\beta}{M} + \frac{vL \cos \beta}{N} \right) \right)}{\pi \left(\frac{uL sin\beta}{M} + \frac{vL \cos \beta}{N} \right)}$$
$$\times exp \left[-2j\pi (\frac{ux_0(t)}{M} + \frac{vy_0(t)}{N}) \right] \quad (17)$$

where M and N represent the width and height of the star image, L is the motion blurred length, β is the motion blurred angle, as shown in Fig.6.

In optical images, point impulse is a bright spot in the dark background, whose two-dimensional impulse response is the point spread function. Therefore, in our paper, the star point can be expressed by the point impulse $\delta(x, y)$. A star point becomes a line segment due to motion blur. From the nature of the impulse function, the Fourier transform of the impulse function is 1.

Without considering the influence of noise, (15) can be turned into

$$G(u, v) = H(u, v) \quad (18)$$

The line segment at this time represents the point spread function during the degradation process. Fig.5 shows a point spread function model with the motion blurred angle of zero degrees and the motion blurred length of 10. Therefore, we only need to study the parameters of the blurred image to estimate the point spread function. For the blur caused by uniform linear motion, the point spread function is

$$h(x.y) = \frac{1}{L} \prod_L (x \cos \beta + y \sin \beta) \quad (19)$$

$\prod_L (u)$ is a rectangle function defined by

$$\prod_L (u) = \begin{cases} 1 & (|u| \le \frac{L}{2}) \\ 0 & (|u| \ge \frac{L}{2}) \end{cases} \tag{20}$$

It can be seen from (20) that the estimation of the point spread function mainly depends on two parameters: motion blurred length and motion blurred angle.

1) ESTIMATION OF MOTION BLURRED ANGLE

Since the star point is a uniform linear motion during a short exposure time, that is, blurring occurs along the moving direction, the distance perpendicular to the moving direction is the shortest for the blurred process.

In the process of finding the MBR of the space target, when we determine the direction of the major axis, we minimize P respect to θ. Whether the space target is translated, rotated or scaled, the calculation method of the major axis direction is invariable. Therefore the direction of the major axis is the direction of motion blurred angle, and the motion blurred angle is given by

$$\beta = arctan \frac{y_4 - y_3}{x_4 - x_3} \tag{21}$$

2) ESTIMATION OF MOTION BLURRED LENGTH

Motion blurring can be understood as the ''tailing'' phenomenon caused by the overlapping of pixels in the motion process. Then each pixel overlaps with the previous cell position during the motion, and the overlapping distance is the motion blurred length. It is known from the motion blurred angle estimation that the direction of the main axis is the direction of the blurred angle. Since the main axis passes through the centroid, the long side length of the MBR corresponding to the main axis direction is the blurred length. Therefore the motion blurred length is calculated by

$$L = \sqrt{(x_4 - x_3)^2 + (y_4 - y_3)^2} \tag{22}$$

D. IMAGE RESTORATION BASED ON REGULARIZATION

In recent years, with the introduction of the image sparse representation theory, it has been found that the proportion of abrupt scenes in star images is small like that in natural images. Therefore, the sparse prior information of the image can be used to guide the sparse regularization restoration of the image.

Once the point spread function $h(x, y)$ of the finest level has been estimated, we can use method in [37], which is fast and robust to small kernel errors, to recover the blurred star image to obtain target image $f(x, y)$ from $h(x, y)$ and $g(x, y)$. This algorithm uses a continuation method to solve the following cost function:

$$\min_{f} \alpha \|f(x, y) * h(x, y) - g(x, y)\|_2^2$$
$$+ \|\nabla_x g(x, y)\|_{1+} \|\nabla_y g(x, y)\|_1 \tag{23}$$

FIGURE 7. A 40-cm horizontal optical telescope.

TABLE 1. Parameters of telescope.

Parameter	Value
Aperture of telescope	400 mm
Size of frame	512 pixels ×512 pixels
CCD operating mode	Full frame
Range of star index	Near-earth target 11 star index
	Hear-earth orbit target 5 star index
Detection accuracy	3rms
Timing accuracy	0.1ms
Mechanical	None

where, $h(x, y)$ is the PSF that we figured out before, $f(x, y)$ is the currently estimated recovered image, ∇_x and ∇_y are regularizing operators, α is the weight. The resulting image $f(x, y)$ is used as the input of the next iteration until the number of iterations is satisfied. The output is the restored image.

IV. EXPERIMENTAL RESULTS

In order to verify the effectiveness of the proposed blind deblurring algorithm comprehensively, the experiments are based on both simulation and real star images. Testing of this algorithm was carried out in the Windows 8 system, using matlabR2017b environment in a 64-bit address space and the experimental machine is stored as 8G.

The real images are provided by the Changchun Satellite Observatory of the National Astronomical Observatory of the Chinese Academy of Sciences. A 40-cm horizontal optical telescope on an alt-azimuth mounting is used in our experiments, which is shown in Fig.7. The telescope is dedicated for surveying space target, and the parameters of the telescope are shown in Table 1. The space targets are the MEO space targets.

A. PERFORMANCE OF SALIENCY DETECTION

Fig. 8 shows the results after saliency detection filtering. Three groups of real space target images are selected in the experiment which are provided by the Changchun Satellite Observatory of the National Astronomical Observatory of the Chinese Academy of Sciences. The parameters are same as
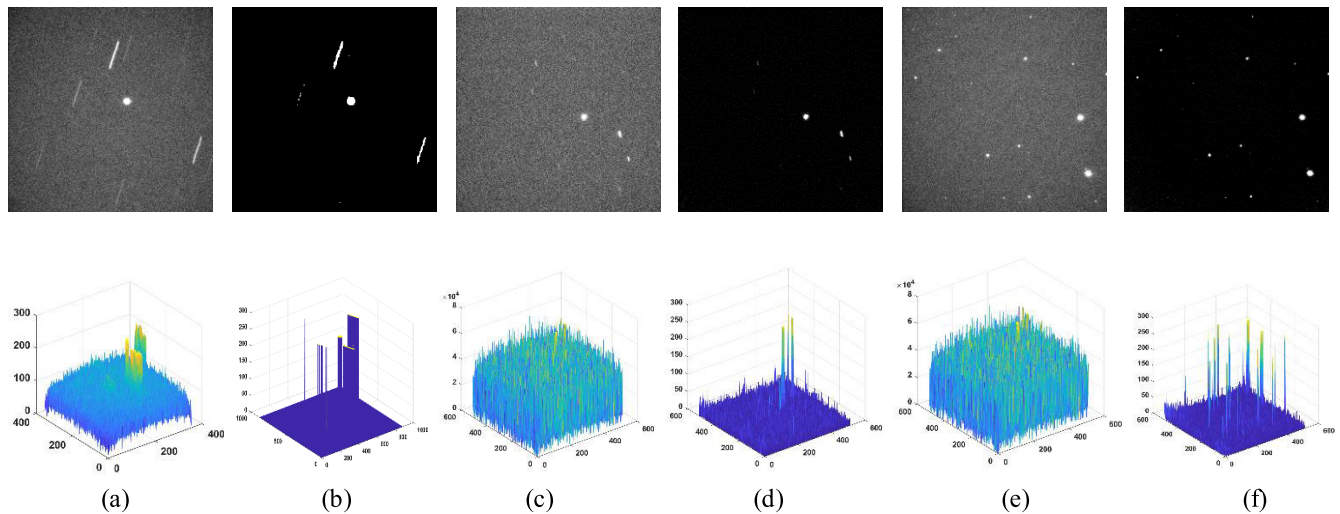
FIGURE 8. Results of saliency detection; (a) (c) (e) Original star images; (b) (d) (f) Saliency-detected images.
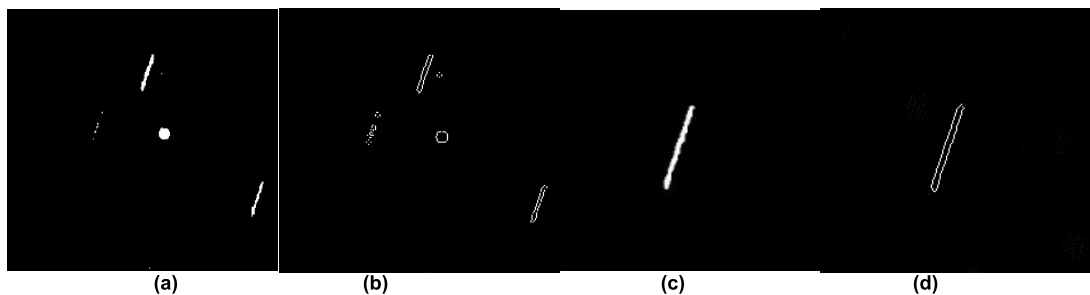

FIGURE 9. Results of edge detection; (a) (c) Original star images after saliency detection; (b) (d) Edge-detected star images.
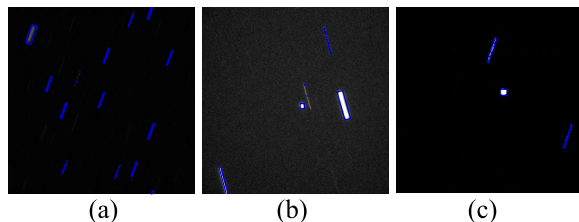

FIGURE 10. Three images of space targets described by the MBR.(a) Space target image ①; (b) Space target image ②;(c) Space target image ③.

those in Table 1. The size of the star image is 512×512. It can be seen from Fig.8 that the noise is large, and the energy of the blurred star image is distributed in the adjacent pixels, among which a few targets are almost embedded into the background noise, and the signal-to-noise ratio is very low. The contrast between the target and background is difficult to meet the subsequent detection and deblurring due to the weak dark space target. After performing the saliency detection as shown in Fig.8 (b), (d), (f), the image contrast is significantly increased and most of the noise has been filtered out, leaving only stars and space targets.

B. EDGE DETECTION
Edge detection based on Canny operator is needed for the image after saliency detection to assist the subsequent

recognition and deblurring of space target image. In order to show the effectiveness of edge detection for small and weak targets, the following experiments are carried out.

In our experiments the size of the blurred star image is 512×512. The upper and lower limits of the threshold of edge detection are 0.9 and 0.5 respectively. Fig. 9 gives the results of space target edge detection. Fig. 9 (a) (c) are the original star images after saliency detection; Fig. 9 (b) (d) are edge-detected star images. It can be seen that the edge is thinner and the edge line is continuous after canny operation. The positioning accuracy of edge detection is mainly reflected in the estimation of point spread function. Therefore, we will show it in subsequent experiments.

Figure.10 are three space targets identified by the MBR. We can see that almost all space targets are identified and marked with blue rectangles.

C. RESULTS OF POINT SPREAD FUNCTION ESTIMATION
In the simulation experiments, in order to meet the requirements of the space targets detection accuracy simulation, and the exposure time T of the star sensor is 1.5s, the imaging area array size is 512 pixels × 512 pixels, the lens focal length is 60 cm, the star sensitivity is 5 Mv, and the rotational angular velocity is 10 ° / s.
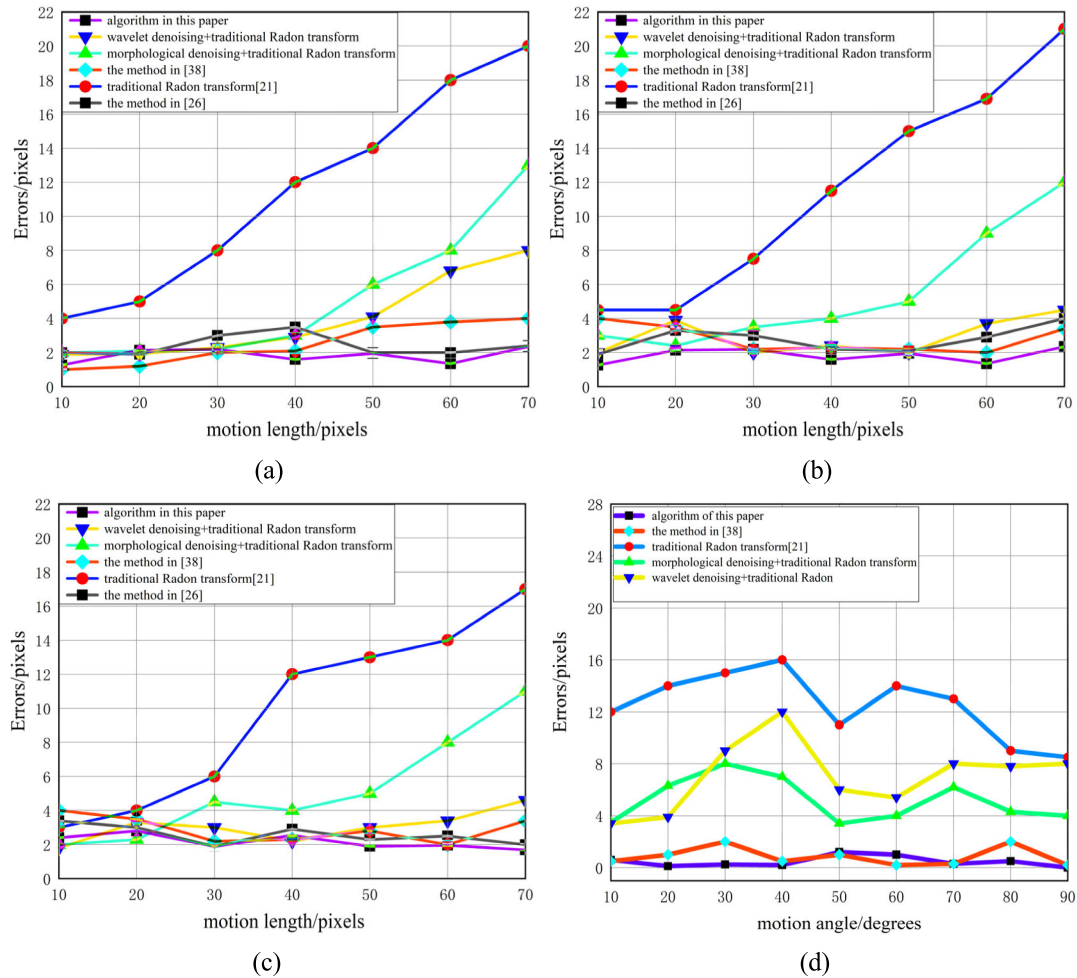
FIGURE 11. Results of different estimation algorithms; (a) (b) (c) errors with different motion lengths (d) errors with different motion angles.

The motion blurred star image used in this part is simulated under the noise with zero mean and mean square error of 0.1. The traditional Radon transform [21], the traditional Radon transform combined with different denoising algorithm, the method in [38], the method in [26] and the method in this paper are applied to the estimation of motion parameters respectively.

In the experiment, the parameter estimation error is utilized to evaluate the performance of our proposed method. The estimation error of motion blurred parameters is the difference between the estimated motion blurred parameters obtained from the experiment and the motion blurred parameters set by the original blurred star images. Detail error analysis data is shown in the Fig.11. The experimental conditions are as follows: in Fig.11 (a), the blurred angle is fixed at 10°, and the blurred distance is changed from 10 pixels to 70 pixels. In Fig.11 (b), the blurred angle is fixed at 20°, and the blurred distance is changed from 10 pixels to 70 pixels. In Fig.11 (c), the blurred angle is fixed at 10°, and the blurred distance is changed from 10 pixels to 70 pixels. As for Fig.10 (d), the length blurred is fixed at 40 pixels, and the range in the angle of motion blur is from 10° to 90°.

It can be seen from Fig.11 that there is no correlation between the increase of the motion angle and the estimation error. However, the estimation error will increase as the motion distance increases. The error of the proposed method is significantly smaller than that of the algorithms in [21], [38] and [26], especially when the motion blurred length and motion blurred angle are large. When the motion blurred length is fixed, motion blurred angle error is within 0° to 2 °; when the motion blurred angle is fixed, the error range of the motion blurred length is between 0 pixel and 1 pixel. The errors of the proposed method decrease dramatically comparing with the methods in [21], [38] and [26]. Therefore our algorithm can better estimate the point spread function and ensure the robustness of the algorithm.

D. ANALYSIS OF RESTORATION RESULTS
1) STAR IDENTIFICATION RESULTS OF A STAR IMAGE FRAME
In order to verify the validation of the proposed method, the star images were captured at Changchun Observatory of National Astronomical Observatories Academy of Science, where there is no stray light from city. The parameters of
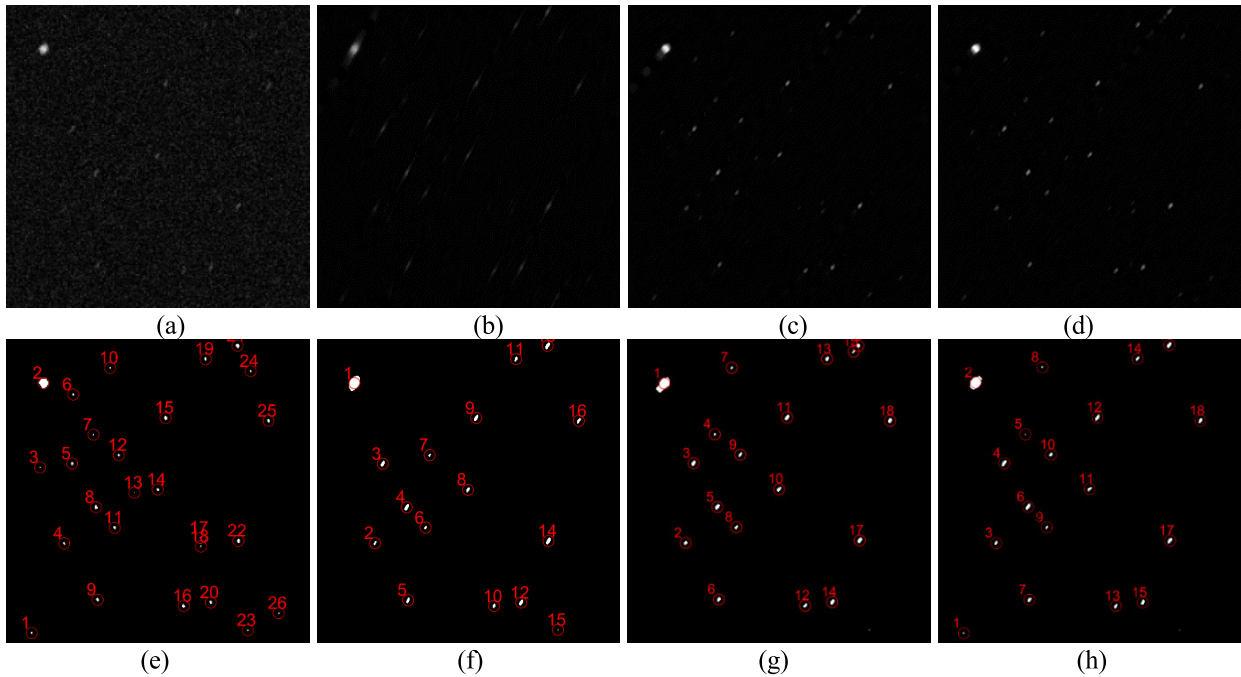
FIGURE 12. (a)Original motion blurred star image; (e) Identification result of the original image; (b) Processed image using method in [28];(f) Identification result using method in [28]; (c) Processed image using method in [26];(g) Identification result using method in [26];(d) Processed image using our method; (h) Identification results using our method. Extracted stars are marked in circles.

the optical telescope used for the shooting are described in Table1. We carried out simulation experiments according to the parameters of the captured images under different dynamic conditions and noise levels. For the method of regularization, the weight α is 3000. The number of iterations is 20.

Fig. 12 (a) shows the simulated star image under dynamic conditions and the parameters of the star image which are shown in Table 2. The exposure time is 90 ms. With the given attitude information, the signal-to-noise ratio (SNR) limit [38], and the motion degradation model [40], [3], we can simulate the motion-blurred star image. The Gaussian white noise with standard deviation 30 (the saturated gray level of a pixel is 65535) to the blurred star image is subsequently added. The star image corresponding to each angular velocity and noise gray level is simulated 50 times randomly, and the average value is taken as the final result. In this way, we can generate motion-blurred star image.

Fig.12 (b), (c), (d) provide the deblurred images using the fuzzy kernel restoration method in [28], [26] and the proposed method respectively. And the identification results are shown in Fig. 12 (f), (g), (h). The star points recovered by the method in [28] have ringing effect, and the brightness of the restored star points is low, which increases the burden of location calculation. It can be seen that the restoration image of method in [26] has a great improvement in star point brightness compared with the method in [28], but there are still many artifacts on the edge. Our algorithm can restore more star points, and increase the brightness of star points.

According to the theory provided by Pascu and Schmidt [41], when there are sufficient background stars, the astronomical positioning accuracy of the object depends on the centering accuracy of the object image. The captured images are affected by the image degradation, which results in the large position errors of star centroid. Therefore, it is unacceptable for practical engineering applications. In our experiments, the recognition rate and the error of the centroid location are used to evaluate the performance of our proposed method. The center of moment method is used to calculate the centroid and the coordinates of star points. The four groups of centroid coordinates shown in Table 2 are calculated from original image, the restored image using method in [28], the restored image using method in [26] and the restored image of our method. Table 2 also shows that the number of the detected stars increases after restoration. As the false detection caused by star blur decreases, the centroid accuracy improves. The number of star points in the original star image is 26 as shown in Fig.12 (e). The number of star points identified by the method in [26] is 16, which is shown in Fig. 11 (f). The number of star points identified by the method in [26] is 17, which is shown in Fig.12 (g). While our algorithm can identify 18 star points which is shown in Fig.12 (h). Therefore, our algorithm has a higher recognition rate. Furthermore, the centroid accuracy of our method is higher. It is vital for the improvement of the centroid accuracy and satellite positioning.

Table 3 gives the accuracy comparison of star point extraction for restored star image. The methods, which

TABLE 2. Star identification results of a star image frame.

Extracted star information			Identified star information						
Star			Original image		Method in [28]		Method in [26]		Our method
NO.	Declina tion/°	Mag./ Mv	x/pixel	y/pixel	x/pixel	y/pixel	x/pixel	y/pixel	x/pixel	y/pixel
1	20.4	3.68	424.024	37.500	Fail	Fail	Fail	fail	424.430	37.500
2	20.5	3.96	64.0228	54.669	64.115	54.621	64.604	54.340	64.046	54.657
3	27.2	4.72	185.504	49.500	Fail	Fail	Fail	Fail	Fail	Fail
4	23.9	5.10	294.924	84.423	294.483	84.672	294.334	84.991	294.789	84.299
5	20.3	5.12	179.971	95.851	180.214	95.629	179.795	96.384	179.980	95.799
6	25.3	4.99	80.422	97.484	Fail	Fail	Fail	Fail	Fail	Fail
7	26.4	4.93	138.467	126.659	Fail	Fail	137.825	126.988	138.506	126.379
8	22.6	4.55	242.938	130.158	243.043	130.082	242.453	130.664	242.958	130.246
9	16.0	3.42	376.143	132.446	376.465	132.361	375.823	132.903	376.200	132.470
10	16.9	4.99	42.008	150.501	42.522	150.731	41.982	151.367	42.106	150.752
11	25.5	5.10	272.378	157.188	272.445	157.431	271.755	157.962	272.197	157.309
12	17.2	5.10	167.773	163.135	168.261	163.053	167.206	163.772	167.755	163.224
13	18.2	4.41	222.000	185.500	Fail	Fail	Fail	Fail	Fail	Fail
14	19.2	4.67	217.436	219.180	217.659	219.052	216.982	219.616	217.390	219.147
15	20.5	4.53	114.194	230.556	114.017	230.574	113.7126	231.127	114.205	230.540
16	24.3	5.15	385.175	256.519	385.192	256.554	384.622	257.271	385.264	256.679
17	28.5	5.10	287.000	280.500	Fail	Fail	Fail	Fail	Fail	Fail
18	24.7	5.17	299.341	281.316	Fail	Fail	Fail	Fail	Fail	Fail
19	29.3	5.29	29.369	288.131	29.472	288.327	29.120	288.883	29.579	288.344
20	16.8	5.33	380.056	295.595	380.221	295.551	379.629	296.286	380.150	295.652
21	19.5	5.47	10.102	334.062	10.034	333.974	10.343	333.904	10.048	333.933
22	29.3	5.55	291.311	335.335	291.446	335.168	290.688	335.885	291.288	335.068
23	27.4	5.59	420.059	348.989	Fail	Fail	Fail	Fail	Fail	Fail
24	23.5	5.60	46.820	352.871	Fail	Fail	Fail	Fail	Fail	Fail
25	17.6	5.57	118.464	378.729	119.178	378.599	118.133	379.417	118.822	378.709
26	18.0	5.80	395.500	393.500	Fail	Fail	Fail	Fail	Fail	Fail

TABLE 3. The average centroid position of different restoration methods.

Parameters	Avg_err_*wnr* [39](pixels)	Avg_err_*RL* [28](pixels)	Avg_err_*lp* [29](pixels)	Avg_err_method [26] (pixels)	Avg_err_prop (pixels)
Average error	(0.448,0.319)	(0.382,0.293)	(0.220,0.269)	(0.167,0.149)	(0.108,0.119)

are the Wiener filter [39], accelerated RL method in [28], l-p regularization [29], and the method in [26], are compared respectively. The parameters are set according to [39], [28], [29], [26]. All of the restoration methods above are with the corrected blur kernel as the common condition. The centroid coordinates of the star points calculated from the restored images are compared with the original centroid coordinates of the star points.

The first column in Table 3 is the result of the Wiener filter [39], which has large error of the centroid position. The second column is the result of the accelerated RL method [28]. The accelerated RL method [28] is robust to noise, but the ringing phenomenon limits its accuracy. The third column is the result of l-p regularization [29], which

solves the ringing phenomenon. Its accuracy is higher than that of the accelerated RL method, however, the overall brightness is low, which limits the accuracy improvement. The forth column is the method in [26]. This method can obtain a higher precision centroid position. The fifth column is the method in this paper, which has the smallest average error of centroid position. Table 3 shows that the reconstructed image is more similar to the truth using the method proposed in this paper, which verifies that the proposed reconstruction method has better performance.

A fuzzy star image with a blurred angle $\theta = 20°$ and a motion blurred length from 10 to 50 pixels is simulated. The centroid extraction accuracy, the number of misidentified stars, the star image recognition failure rate of the blurred

TABLE 4. The accuracy of centroid extraction before and after recovery with L/pixels in the case of $\theta = 20°$.

L	Blurred star image			Restored star image		
	Centroid accuracy /pixels	Number of misidentified stars	Identification error rate /%	Centroid accuracy /pixels	Number of misidentified stars	Identification error rate /%
10	0.3855	1.2554	6.68	0.2033	0.0236	5.21
20	0.4004	1.9874	16.99	0.2445	0.0347	6.15
30	0.5844	3.1459	44.33	0.2834	0.0523	7.35
40	0.7004	4.2599	66.58	0.3123	0.1157	8.74
50	0.7225	5.0113	75.62	0.3566	0.3366	14.06
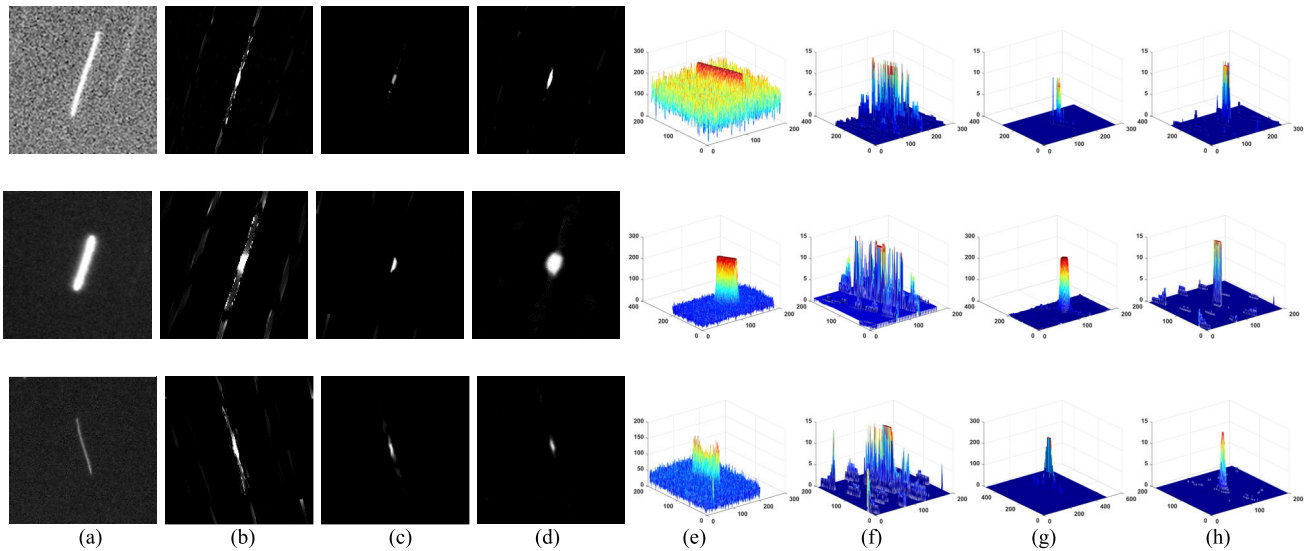
FIGURE 13. Comparison results for different deblurring algorithms; (a)Original star image; (b) Method in literature [21]; (c) Method in literature [38]; (d) Proposed method; (e) 3D image intensity profiles of original star image; (f) 3D image intensity profiles of method in literature [20]; (g) 3D image intensity profiles of method in literature [32]; (h) 3D image intensity profiles of proposed method.

star image, the restored star images compared with different deblurred length are given in Table 4. The centroid extraction accuracy is the average accuracy of the correctly identified star points. The number of misidentified stars refers to the average number of stars in each star image that are not recognized in the star image.

It can be seen from Table 4 that with the increase of the motion length, the accuracy of centroid extraction is declining whether it is a fuzzy star image or a restored star image. In different motion blurred lengths, the recognition error rate and the number of misidentified stars decrease significantly. The recognition error rate is reduced from 75.62% to 14.06% using our method when the motion blurred angle is 20° and the motion blurred length is 50 pixels. It can be observed that the number of misidentified stars decreases from 5.0113 to 0.3366. From this comparison, we can see that our method is more robust to different dynamic conditions. Therefore, the attitude information can be obtained more accurately by the proposed method.

2) RESULTS OF RESTORATION
Fig.13 (a) is the acquired space target image and (e) is the 3D image intensity profiles. Fig. 13 (b), (c), (d) provide the

deblurred images using the fuzzy kernel restoration method in [21], the method in [38], the proposed method respectively. The star point in the Fig.13 (c) has a better restoration effect, but the brightness is still low, which is not beneficial to the subsequent detection. In the Fig.13 (d), after the blind deblurring of the algorithm, the star spot is clarified, the distribution is close to the Gaussian distribution, and the brightness is higher than that of the fuzzy star image. Furthermore, it can be seen that our algorithm reduces the ringing effect in comparison with other two methods. It can be used in a low SNR environment.

V. CONCLUSION
This paper proposes a blind deblurring algorithm capturing space target features. By analyzing the sparse characteristics of the star image, we find the relationship between the degraded image and the restored image. The minimum bounding rectangle algorithm is used to estimate the motion direction and motion length of the space targets and consequently to help the space target restoration. The identification rate and the error of the centroid location are used to evaluate the performance of restoration. The experiments show that the restoration effect is significantly improved. The positioning

accuracy is enhanced and the number of star points recognized is more.

REFERENCES

[1] C. C. Liebe, "Accuracy performance of star trackers—A tutorial," *IEEE Trans. Aerosp. Electron. Syst.*, vol. 38, no. 2, pp. 587–599, Apr. 2002.

[2] H. Wang, W. Zhou, X. Cheng, and H. Lin, "Image smearing modeling and verification for strapdown star sensor," *Chin. J. Aeronaut.*, vol. 25, no. 1, pp. 115–123, Feb. 2012.

[3] C. S. Liu, L. H. Hu, G. B. Liu, B. Yang, and A. J. Liu, "Kinematic model for the space-variant image motion of star sensors under dynamical conditions," *Opt. Eng.*, vol. 54, no. 6, Jun. 2015, Art. no. 063104.

[4] J. L. Jørgensen and C. C. Liebe, "The advanced stellar compass, development and operations," *Acta Astronaut.*, vol. 39, pp. 775–783, Nov./Dec. 1996.

[5] X. Liu, Z. Zhou, Z. Zhang, D. Liu, and X. Zhang, "Improvement of star identification based on star trace in star images," *Measurement*, vol. 105, pp. 158–163, Jul. 2017.

[6] C. Liu, G. Liu, X. Wang, and A. Li, *Principles and Systematic Applications of Missile-Borne Star Sensor*. Beijing, China: Nat. Defense Ind., 2010, pp. 194–197.

[7] X. Wei, W. Tan, J. Li, and G. Zhang, "Exposure time optimization for highly dynamic star trackers," *Sensors*, vol. 14, no. 3, pp. 4914–4931, 2014.

[8] D. G. Sheppard, B. R. Hunt, and M. W. Marcellin, "Iterative multi-frame super-resolution algorithms for atmospheric turbulence-degraded imagery," in *Proc. IEEE Int. Conf. Acoust., Speech Signal Process.*, May 1998, pp. 978–992.

[9] H. Zhang, Y. Su, J. Shang, L. Yang, B. Cai, C. Liu, J. Wang, S. X. Zhou, and Z. Zhang, "Accurate star centroid detection for the advanced geosynchronous radiation imager of fengyun-4A," *IEEE Access*, vol. 6, pp. 7987–7999, 2018.

[10] J. Yang, B. Liang, T. Zhang, and J. Song, "A novel systematic error compensation algorithm based on least squares support vector regression for star sensor image centroid estimation," *Sensors*, vol. 11, no. 8, pp. 7341–7363, 2011.

[11] X. Wang, X. Wei, Q. Fan, J. Li, and G. Wang, "Hardware implementation of fast and robust star centroid extraction with low resource cost," *IEEE Sensors J.*, vol. 15, no. 9, pp. 4857–4865, Sep. 2015.

[12] K. R. Castleman, *Digital Image Processing*. Upper Saddle River, NJ, USA: Prentice-Hall, 1998.

[13] J. L. Starck and F. Murtagh, *Astronomical Image and Data Analysis*. Berlin, Germany: Springer, 2006, pp. 71–111.

[14] T. R. Bontekoe, E. Koper, and D. J. M. Kester, "Pyramid maximum entropy images of IRAS survey data," *Astron. Astrophys.*, vol. 284, no. 3, pp. 1037–1053, 1994.

[15] D. Alloin, E. Pantin, P. O. Lagage, and G. L. Granato, "0.6 resolution images at 11 and 20 mu m of the active galactic nucleus in NGC 1068," *Astron. Astrophys.*, vol. 363, no. 3, pp. 926–932, 2000.

[16] Z.-H. Tang, S.-H. Wang, and W.-J. Jin, "Removal of tracking error with image restoration," *Astron. J.*, vol. 121, no. 2, pp. 1199–1206, 2001.

[17] B. L. Mcglamery, "Restoration of turbulence-degraded images," *J. Opt. Soc. Amer.*, vol. 57, no. 99, pp. 293–296, 1967.

[18] C. W. Helstrom, "Image restoration by the method of least squares," *J. Opt. Soc. Amer.*, vol. 57, no. 3, pp. 297–303, 1967.

[19] X. Wu and X. Wang, "Multiple blur of star image and the restoration under dynamic conditions," *Acta Astronaut.*, vol. 68, nos. 11–12, pp. 1903–1913, Jun./Jul. 2011.

[20] W. Zhang, W. Quan, and L. Guo, "Blurred star image processing for star sensors under dynamic conditions," *Sensors*, vol. 12, no. 5, pp. 6712–6726, 2012.

[21] T. Sun, F. Xing, Z. You, X. Wang, and B. Li, "Smearing model and restoration of star image under conditions of variable angular velocity and long exposure time," *Opt. Express*, vol. 22, no. 5, pp. 6009–6024, 2014.

[22] L. Ma, D. Zhan, G. Jiang, S. Fu, H. Jia, X. Wang, Z. Huang, J. Zheng, F. Hu, W. Wu, and S. Qin, "Attitude-correlated frames approach for a star sensor to improve attitude accuracy under highly dynamic conditions," *Appl. Opt.*, vol. 54, no. 25, pp. 7559–7566, 2015.

[23] K. Wang, C. Zhang, Y. Li, and X. Kan, "A new restoration algorithm for the smeared image of a SINS-aided star sensor," *J. Navigat.*, vol. 67, pp. 881–898, May 2014.

[24] H. Zhang, Y. X. Niu, J. Z. Lu, and Y. Q. Yang, "System-level calibration for the star sensor installation error in the stellar-inertial navigation system on a swaying base," *IEEE Access*, vol. 6, pp. 47290–47294, 2018.

[25] B. D. Jeffs and M. Gunsay, "Restoration of blurred star field images by maximally sparse optimization," *IEEE Trans. Image Process.*, vol. 2, no. 2, pp. 202–211, Apr. 1993.

[26] S. Wang, S. Zhang, M. Ning, and B. Zhou, "Motion blurred star image restoration based on MEMS Gyroscope aid and blur kernel correction," *Sensors*, vol. 18, no. 8, p. 2662, 2018.

[27] D. Liu, X. Chen, X. Liu, and C. Shi, "Star image prediction and restoration under dynamic conditions," *Sensors*, vol. 19, no. 8, p. 1890, 2019.

[28] L. Ma, F. Bernelli-Zazzera, G. Jiang, X. Wang, Z. Huang, and S. Qin, "Region-confined restoration method for motion-blurred star image of the star sensor under dynamic conditions," *Appl. Opt.*, vol. 55, no. 17, pp. 4621–4631, 2016.

[29] C. Zhang, J. Zhao, T. Yu, H. Yuan, and F. Li, "Fast restoration of star image under dynamic conditions via ℓ_p regularized intensity prior," *Aerosp. Sci. Technol.*, vol. 61, pp. 29–34, Feb. 2016.

[30] J. Zhao, C. Zhang, and T. Yu, "Accuracy enhancement of navigation images using blind restoration method," *Acta Astronaut.*, vol. 142, pp. 193–200, Jan. 2018.

[31] A. A. Ramos, J. de la Cruz Rodríguez, and A. P. Yabar, "Real-time multi-frame blind deconvolution of solar images," *Astron. Astrophys.*, vol. 620, p. A73, Dec. 2018.

[32] D. Krishnan and R. Fergus, "Fast image deconvolution using hyper-Laplacian priors," in *Proc. Int. Conf. Neural Inf. Process. Syst.*, 2009, pp. 1033–1041.

[33] W. Souidene, K. Abed-Meraim, and A. Beghdadi, "A new look to multi-channel blind image deconvolution," *IEEE Trans. Image Process.*, vol. 18, no. 7, pp. 1487–1500, Jul. 2009.

[34] B. Gou and Y. Cheng, "Automatic centroid extraction method for noisy star image," *IET Image Process.*, vol. 12, no. 6, pp. 856–862, 2018.

[35] Y. Zhai and M. Shah, "Visual attention detection in video sequences using spatiotemporal cues," in *Proc. ACM Int. Conf. Multimedia*, Santa Barbara, CA, USA, 2006, pp. 815–824.

[36] C. Sha, X. Li, Q. Shao, and J. Wu, and S. Bian, "Saliency detection via boundary and center priors," in *Proc. Int. Congr. Image Signal Process.*, Dec. 2014, pp. 1066–1071.

[37] D. Krishnan, T. Tay, and R. Fergus, "Blind deconvolution using a normalized sparsity measure," in *Proc. IEEE Comput. Vis. Pattern Recognit.*, Jul. 2011, vol. 42, no. 7, pp. 233–240.

[38] J. Jiang, J. N. Huang, and G. J. Zhang, "An accelerated motion blurred star restoration based on single image," *IEEE Sensors J.*, vol. 17, no. 5, pp. 1306–1315, Mar. 2017.

[39] Q. Wei and Z. Weina, "Restoration of motion-blurred star image based on Wiener filter," in *Proc. Int. Conf. Intell. Comput. Technol. Autom. (ICICTA)*, Mar. 2011, pp. 691–694.

[40] J. Shen, G. Zhang, and X. Wei, "Simulation analysis of dynamic working performance for star trackers," *J. Opt. Soc. Amer. A, Opt. Image Sci. Vis.*, vol. 2, no. 12, pp. 2638–2647, 2010.

[41] D. Pascu and R. E. Schmidt, "Photographic positional observations of Saturn," *Astron. J.*, vol. 99, no. 6, pp. 1974–1984, 1990.

PEIYU LIU was born in Jilin, China, in 1996. She received the B.S. degree in communication engineering from Jilin University, Changchun, China, in 2018, where she is currently pursuing the M.S. degree with the Communication Engineering School.

Her research interests include image processing, image restoration, and star image recognition.

YAN ZHAO (M'10) was born in Jilin, China, in 1971. She received the B.S. degree in communication engineering from the Changchun Institute of Posts and Telecommunications, in 1993, the M.S. degree in communication and electronic from the Jilin University of Technology, in 1999, and the Ph.D. degree in communication and information system from Jilin University, in 2003.

She was a Postdoctoral Researcher with the Digital Media Institute, Tampere University of Technology, Finland, from March 2003 to December 2003. From March 2008 to August 2008, she was a Visiting Professor with the Institute of Communications and Radio-Frequency Engineering, Vienna University of Technology. She is currently a Professor with the College of Communication Engineering. Her research interests include image and video processing, multimedia signal processing, and error concealment for audio and video transmitted over unreliable networks.

SHIGANG WANG was born in Jilin, China, in 1962. He received the B.S. degree from Northeastern University, in 1983, the M.S degree in communication and electronic from the Jilin University of Technology, in 1998, and the Ph.D. degree in communication and information system from Jilin University, in 2001.

He is currently a Professor with the College of Communication Engineering. His research interests include image and video coding, multidimensional signal processing, and stereoscopic and multi-view video coding.

WENBO YANG was born in Jilin, China, in 1980. He received the Ph.D. degree from the Changchun Institute of Optics, Fine Mechanics and Physics, Chinese Academy of Sciences, in 2014. He is currently pursuing the Ph.D. degree with the College of Communication Engineering, Jilin University. He is currently an Assistant Researcher with the Changchun Satellite Observation Station of National Astronomical Observatories, Chinese Academy of Sciences.

He is mainly engaged in research on astrometry and automatic control.

SHU CHEN received the B.S. degree in applied mathematics from Northeastern University, Shenyang, China, in 2013. She is currently pursuing the M.S. degree with the College of Communication Engineering, Jilin University, Changchun, China.

She was an Assistant with the Special Equipment Teaching and Research Office, Intelligence Investigation Department, Special Police College of PAP, Beijing. Her research interests include image processing and integrated imaging.

• • •